3-3-2011

Coherent Photoproduction of π^+ from 3He

R. Nasseripour

Gerard P. Gilfoyle
University of Richmond, ggilfoyl@richmond.edu

et. al.

Recommended Citation

Nasseripour, R., B. I. Berman, K. P. Adhikari, D. Adikaram, M. Anghinolfi, J. Ball, M. Battaglieri, V. Batourine, I. Bedlinskiy, A. S. Biselli, D. Branford, W. J. Briscoe, W. K. Brooks, V. D. Burkert, D. S. Carman, L. Casey, P. I. Cole, P. Collins, V. Crede, A. D'Angelo, A. Daniel, N. Dashyan, R. De Vita, E. De Sanctis, A. Deur, B. Dey, R. Dickson, C. Djalali, D. Doughty, R. Dupre, H. Egiyan, A. El Alaoui, L. El Fassi, S. Fegan, A. Fradi, M. Y. Gabrielyan, G. P. Gilfoyle, K. I. Giovanetti, F. X. Girod, J. T. Goetz, W. Gohn, R. W. Gothe, L. Graham, K. A. Griffioen, B. Guegan, K. Hafidi, H. Hakobyan, C. Hanretty, D. Heddle, M. Holtrop, C. E. Hyde, Y. Ilieva, D. G. Ireland, E. I. Isupov, D. Keller, M. Khandaker, P. Khetarpal, A. Kim, W. Kim, A. Klein, F. J. Klein, P. Konczykowski, V. Kubarovsky, S. E. Kuhn, S. V. Kuleshov, V. Kuznetsov, N. D. Kvaltine, K. Livingston, H. Y. Lu, I. J.D. Macgregor, M. Mayer, J. Mcandrew, B. Mckinnon, A. M. Micherdzinska, M. Mirazita, K. Moriya, B. Moreno, B. Morrison, H. Moutarde, E. Munevar, P. Nadel-Turonski, A. Ni, S. Niccolai, G. Niculescu, I. Niculescu, M. Osipenko, A. I. Ostrovidov, M. Paolone, R. Paremuzyan, K. Park, S. Park, E. Pasyuk, S. Pereira, Y. Perrin, S. Pisano, S. Pozdniakov, J. W. Price, S. Procureur, D. Protopopescu, M. Ripani, B. G. Ritchie, G. Rosner, P. Rossi, F. Sabatié, M. S. Saini, C. Salgado, D. Schott, R. A. Schumacher, H. Seraydaryan, Y. G. Sharabian, E. S. Smith, G. D. Smith, D. I. Sober, D. Sokhan, S. S. Stepanyan, S. Stepanyan, P. Stoler, S. Strauch, R. Suleiman, M. Taiuti, W. Tang, C. E. Taylor, D. J. Tedeschi, S. Tkachenko, M. Ungaro,

Coherent photoproduction of π^+ from ^{3}He

R. Nasseripour,[1] B.L. Berman,[1] K.P. Adhikari,[30] D. Adikaram,[30] M. Anghinolfi,[19] J. Ball,[9] M. Battaglieri,[19] V. Batourine,[36] I. Bedlinskiy,[22] A.S. Biselli,[13,31] D. Branford,[12] W.J. Briscoe,[1] W.K. Brooks,[38,36] V.D. Burkert,[36] D.S. Carman,[36] L. Casey,[8] P.L. Cole,[17,36] P. Collins,[8] V. Crede,[15] A. D'Angelo,[20,33] A. Daniel,[29] N. Dashyan,[42] R. De Vita,[19] E. De Sanctis,[18] A. Deur,[36] B. Dey,[7] R. Dickson,[7] C. Djalali,[35] D. Doughty,[10] R. Dupre,[2] H. Egiyan,[36,41] A. El Alaoui,[2] L. El Fassi,[2] S. Fegan,[39] A. Fradi,[21] M.Y. Gabrielyan,[14] G.P. Gilfoyle,[32] K.L. Giovanetti,[23] F.X. Girod,[36] J.T. Goetz,[4] W. Gohn,[11] R.W. Gothe,[35] L. Graham,[35] K.A. Griffioen,[41] B. Guegan,[21] K. Hafidi,[2] H. Hakobyan,[38,42] C. Hanretty,[15] D. Heddle,[10,36] M. Holtrop,[27] C.E. Hyde,[30] Y. Ilieva,[35] D.G. Ireland,[39] E.L. Isupov,[34] D. Keller,[29] M. Khandaker,[28] P. Khetarpal,[14] A. Kim,[24] W. Kim,[24] A. Klein,[30] F.J. Klein,[8,36] P. Konczykowski,[9] V. Kubarovsky,[36] S.E. Kuhn,[30] S.V. Kuleshov,[38,22] V. Kuznetsov,[24] N.D. Kvaltine,[40] K. Livingston,[39] H.Y. Lu,[7] I.J.D. MacGregor,[39] M. Mayer,[30] J. McAndrew,[12] B. McKinnon,[39] A.M. Micherdzinska,[1] M. Mirazita,[18] K. Moriya,[7] B. Moreno,[9] B. Morrison,[3] H. Moutarde,[9] E. Munevar,[1] P. Nadel-Turonski,[36] A. Ni,[24] S. Niccolai,[21,1] G. Niculescu,[23,29] I. Niculescu,[23,1] M. Osipenko,[19] A.I. Ostrovidov,[15] M. Paolone,[35] R. Paremuzyan,[42] K. Park,[36,24] S. Park,[15] E. Pasyuk,[36,3] S. Anefalos Pereira,[18] Y. Perrin,[25] S. Pisano,[21] S. Pozdniakov,[22] J.W. Price,[5] S. Procureur,[9] D. Protopopescu,[39] M. Ripani,[19] B.G. Ritchie,[3] G. Rosner,[39] P. Rossi,[18] F. Sabatié,[9,30] M.S. Saini,[15] C. Salgado,[28] D. Schott,[14] R.A. Schumacher,[7] H. Seraydaryan,[30] Y.G. Sharabian,[36,42] E.S. Smith,[36] G.D. Smith,[39] D.I. Sober,[8] D. Sokhan,[21] S.S. Stepanyan,[24] S. Stepanyan,[36,42] P. Stoler,[31] S. Strauch,[35] R. Suleiman,[26] M. Taiuti,[16,*] W. Tang,[29] C.E. Taylor,[17] D.J. Tedeschi,[35] S. Tkachenko,[35] M. Ungaro,[11,31] B. Vernarsky,[7] M.F. Vineyard,[37,32] E. Voutier,[25] D.P. Watts,[12] L.B. Weinstein,[30] D.P. Weygand,[36] M.H. Wood,[6] B. Zhao,[41] and Z.W. Zhao[40]

(The CLAS Collaboration)

[1]*The George Washington University, Washington, DC 20052, USA*
[2]*Argonne National Laboratory, Argonne, Illinois 60441, USA*
[3]*Arizona State University, Tempe, Arizona 85287-1504, USA*
[4]*University of California at Los Angeles, Los Angeles, California 90095-1547, USA*
[5]*California State University, Dominguez Hills, Carson, California 90747, USA*
[6]*Canisius College, Buffalo, New York 14208, USA*
[7]*Carnegie Mellon University, Pittsburgh, Pennsylvania 15213, USA*
[8]*Catholic University of America, Washington, DC 20064, USA*
[9]*CEA, Centre de Saclay, Irfu/Service de Physique Nucléaire, F-91191 Gif-sur-Yvette, France*
[10]*Christopher Newport University, Newport News, Virginia 23606, USA*
[11]*University of Connecticut, Storrs, Connecticut 06269, USA*
[12]*Edinburgh University, Edinburgh EH9 3JZ, United Kingdom*
[13]*Fairfield University, Fairfield, Connecticut 06824, USA*
[14]*Florida International University, Miami, Florida 33199, USA*
[15]*Florida State University, Tallahassee, Florida 32306, USA*
[16]*Università di Genova, I-16146 Genova, Italy*
[17]*Idaho State University, Pocatello, Idaho 83209, USA*
[18]*Istituto Nazionale di Fisica Nucleare, Laboratori Nazionali di Frascati, I-00044 Frascati, Italy*
[19]*Istituto Nazionale di Fisica Nucleare, Sezione di Genova, I-16146 Genova, Italy*
[20]*Istituto Nazionale di Fisica Nucleare, Sezione di Roma Tor Vergata, I-00133 Rome, Italy*
[21]*Institut de Physique Nucléaire Orsay, Orsay, France*
[22]*Institute of Theoretical and Experimental Physics, Moscow 117259, Russia*
[23]*James Madison University, Harrisonburg, Virginia 22807, USA*
[24]*Kyungpook National University, Daegu 702-701, Republic of Korea*
[25]*Laboratoire de Physique Subatomique et de Cosmologie de Grenoble, Universite Joseph Fourier, CNRS/IN2P3, Institut Polytechnique de Grenoble, Grenoble, France*
[26]*Massachusetts Institute of Technology, Cambridge, Massachusetts 02139-4307, USA*
[27]*University of New Hampshire, Durham, New Hampshire 03824-3568, USA*
[28]*Norfolk State University, Norfolk, Virginia 23504, USA*
[29]*Ohio University, Athens, Ohio 45701, USA*
[30]*Old Dominion University, Norfolk, Virginia 23529, USA*
[31]*Rensselaer Polytechnic Institute, Troy, New York 12180-3590, USA*
[32]*University of Richmond, Richmond, Virginia 23173, USA*
[33]*Universita' di Roma Tor Vergata, I-00133 Rome, Italy*
[34]*Skobeltsyn Nuclear Physics Institute, Skobeltsyn Nuclear Physics Institute, 119899 Moscow, Russia*
[35]*University of South Carolina, Columbia, South Carolina 29208, USA*
[36]*Thomas Jefferson National Accelerator Facility, Newport News, Virginia 23606, USA*
[37]*Union College, Schenectady, New York 12308, USA*
[38]*Universidad Técnica Federico Santa María, Casilla 110-V Valparaíso, Chile*

[39] *University of Glasgow, Glasgow G12 8QQ, United Kingdom*
[40] *University of Virginia, Charlottesville, Virginia 22901, USA*
[41] *College of William and Mary, Williamsburg, Virginia 23187-8795, USA*
[42] *Yerevan Physics Institute, 375036 Yerevan, Armenia*
(Received 2 November 2010; published 3 March 2011)

We have measured the differential cross section for the $\gamma^3\mathrm{He} \rightarrow \pi^+ t$ reaction. This reaction was studied using the Continuous Electron Beam Accelerator Facility (CEBAF) Large Acceptance Spectrometer (CLAS) at Jefferson Lab. Real photons produced with the Hall-B bremsstrahlung tagging system in the energy range from 0.50 to 1.55 GeV were incident on a cryogenic liquid ^{3}He target. The differential cross sections for the $\gamma^3\mathrm{He} \rightarrow \pi^+ t$ reaction were measured as a function of photon-beam energy and pion-scattering angle. Theoretical predictions to date cannot explain the large cross sections except at backward angles, showing that additional components must be added to the model.

DOI: 10.1103/PhysRevC.83.034001 PACS number(s): 25.20.Lj, 13.60.Le, 21.45.Ff, 25.10.+s

I. INTRODUCTION

Comparing an elementary meson production process on a free nucleon with the same process inside a nucleus is an interesting problem in nuclear physics. The contribution of mesonic degrees of freedom to the various processes in nuclei can be investigated in the case of the two- and three-nucleon systems for which accurate wave functions, based on realistic nucleon-nucleon potentials, are available. Studying this production process is ideal for understanding the interaction of pions with nuclei and to search for possible effects mediated by nucleon resonances in nuclear matter. Reactions such as $\gamma + {}^3\mathrm{He} \rightarrow \pi^+ + t$, $\gamma + {}^3\mathrm{He} \rightarrow \pi^0 + {}^3\mathrm{He}$, $\gamma + t \rightarrow \pi^- + {}^3\mathrm{He}$, and $\gamma + t \rightarrow \pi^0 + t$ have been studied by both experimental and theoretical groups over the last four decades [1–10]. Studying these processes is useful in developing our understanding of nuclear structure and the long-range part of the nucleon-nucleon interaction described by the one-pion exchange model. Furthermore, it provides information to characterize the mechanisms of photon-induced reactions in few-body nucleon systems, for example, the two- and three-body photon-absorption mechanisms and the contributions of the meson-exchange currents (MECs) in these reactions. However, all the previous measurements were done near the threshold or in the Δ resonance region.

This measurement is part of a program at Jefferson Lab to study the mechanisms of photon-induced reactions in few-body systems. This program aims to investigate the fundamental processes in the nuclear environment and to test the theoretical calculations that are performed using the exact few-body nuclear wave functions based on nucleon-nucleon interactions.

The goal of the present analysis is to measure the differential cross section for the $\gamma + {}^3\mathrm{He} \rightarrow \pi^+ + t$ reaction for energies above the Δ resonance region. This analysis is complementary to the previously reported measurements on three-body systems, e.g., the three-body photodisintegration of ^{3}He [11]. The $\gamma + {}^3\mathrm{He} \rightarrow \pi^+ + t$ channel is one of the most important pion-production channels because it is an isoelastic nuclear transition within the isodoublet (^{3}H,^{3}He), with the same quantum numbers as the elementary reaction on the nucleon. The same nuclear wave functions can be used for the initial and final states (except for Coulomb effects). This reaction is particularly attractive because the ^{3}He target is the lightest nucleus on which one can observe coherent π^+ photoproduction with charge exchange. It allows us to study pion photoproduction in a complex nucleus where the final state, consisting of a free pion and triton, is well defined and can be identified easily in terms of energy and angle or momentum transfer.

The first experiment to measure the cross section for $\gamma + {}^3\mathrm{He} \rightarrow \pi^+ + t$ over a range of energies and angles was performed by O'Fallon *et al.* in 1965 [1]. The measurement was done for photon energies of 180–260 MeV and triton scattering angles of 26, 30, 35, and 40 deg. They found that the cross section could be described by the cross section from a single free proton times the square of the nuclear matter form factor for ^{3}He, modified by kinematic factors. However, the measured cross sections were from 25%–50% below the simple form-factor theory. It was suggested that this discrepancy was due to a suppression of pion production in nuclear matter.

In 1979, Argan *et al.* [2] measured the yield of π^+ photoproduction on ^{3}He near the threshold and compared it with electron-scattering data on the proton. They obtained the matrix element for threshold pion photoproduction and showed that a unique form factor cannot account for both processes. This suggested that many-body contributions affect the two reactions differently. In fact, to achieve a complete coherent calculation and to obtain quantitative information on the many-body contribution to pion photoproduction, it was suggested that the ^{3}He and the deuterium cases must be treated in parallel. On the other hand, the pion production can be considered as an almost one-body process where the contribution of Final-state interaction (FSI) is small. In the Δ-resonance region it may be described by the dominance and propagation of that resonance.

Another earlier experiment that measured the differential cross section for $\gamma + {}^3\mathrm{He} \rightarrow \pi^+ + t$ was performed by Bachelier *et al.* [3] in 1973. In that experiment, the differential cross section was measured at a constant value of the momentum transfer of the recoiling triton using the bremsstrahlung photon beam (227.5–453 MeV) of the Saclay linear electron

[*] Current address: Istituto Nazionale di Fisica Nucleare, Sezione di Genova, 16146 Genova, Italy.

accelerator. In that work, the experimental results were obtained as a function of the incident-photon energy and compared with the calculations of Lazard and Maric [4].

Bellinghausen *et al.* [5] performed an experiment in Bonn in 1985 where the photoproduction of charged pions on ^{3}He and ^{3}H was measured in the $\Delta(1232)$-resonance region with an incident-photon energy range of 250–450 MeV. The results of that measurement for $\gamma + {}^3\mathrm{He} \rightarrow \pi^+ + t$ were compared with the calculation of Sanchez-Gomez and Pascual [6]. In their model, the photoproduction of pions on nuclei with three nucleons is considered in the elastic channel. Calculations were performed using the impulse approximation and neglecting rescattering effects. These processes were studied for incident photon energies between 200 and 500 MeV in the laboratory frame.

The current analysis is the first to report on the $\gamma + {}^3\mathrm{He} \rightarrow \pi^+ + t$ channel with incident photon energies above 500 MeV. In Sec. II we discuss the development of the model calculations. The description of the experiment and the data analysis procedures, including the event selection, background corrections, study of the detector acceptance, extracting cross sections, and the systematic uncertainties, are given in Sec. III. Section IV contains the results and comparison with the model calculations.

II. MODEL PREDICTIONS

On the theoretical front, a model was developed by Tiator *et al.* [7] based on realistic three-body Faddeev functions in the plane-wave impulse approximation (PWIA). This model used a production process with Born terms, vector meson exchange, and $\Delta(1232)$ excitation. Good agreement was found with low-momentum-transfer data (up to 3.1 fm^{-2}) from Ref. [3]; however, the PWIA could not explain the data at higher momentum transfer.

In a later calculation performed by Kamalov *et al.* [8], the intermediate pion scattering between two nucleons also was taken into account. In this model, the coherent π^0 and π^+ photoproduction and elastic and charge-exchange pion scattering on ^{3}He were calculated in a consistent way. In this model, realistic three-body Faddeev wave functions were used and full nonlocal distorted-wave impulse-approximation (DWIA) results for pion photoproduction were obtained. Comparison with experimental data showed good agreement over a wide range of momentum transfer for the photon energy range between 230 and 450 MeV.

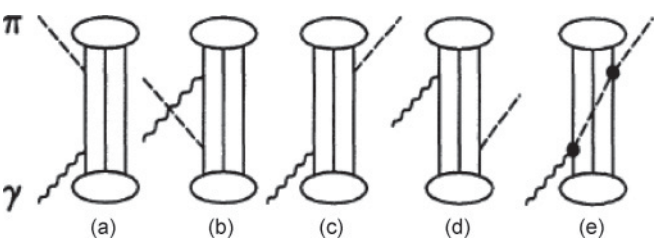

FIG. 1. Diagrams for the dispersive and pion rescattering terms in nuclear pion photoproduction. The two-body diagrams are shown in (c) and (d). Figure is from Ref. [10].

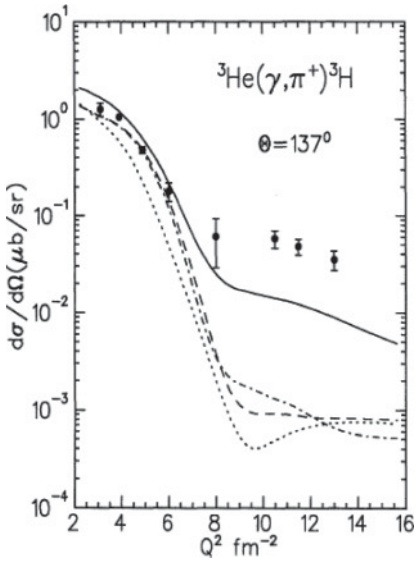

FIG. 2. Differential cross section at $\theta_\pi^{\mathrm{c.m.}} = 137^\circ$ as a function of nuclear momentum transfer Q^2 from Ref. [3]. The dotted (dashed) curves show the PWIA (DWIA) results. The dash-dotted curve includes the corrections due to coupling with the breakup channels, and the solid line shows the complete calculation with the additional two-body mechanisms. Figure is from Ref. [10].

In 1995, the two-body mechanisms were explicitly included in the model [10], where the photon is absorbed by one nucleon and the pion is emitted from the other nucleon (Fig. 1). The inclusion of these processes resulted in better agreement between the calculations and the previous data at higher momentum transfers. However, even with all of the considered effects and pion distortions, the model could not account for the large enhancement seen in the experimental data at large Q^2 ($Q^2 > 6$ fm^{-2}). Figure 2 shows the differential cross section at $\theta_\pi^{\mathrm{c.m.}} = 137^\circ$ as a function of nuclear momentum transfer Q^2 from Ref. [3], compared with the complete model calculations with the additional two-body contributions. The variable Q^2 is the square of the three-momentum of the recoil triton.

III. EXPERIMENT AND DATA ANALYSIS

A. Experimental apparatus

The $\gamma\,{}^3\mathrm{He} \rightarrow t\pi^+$ reaction was measured during CLAS experiment E93-044 (g3a running period) in December 1999 with the Continuous Electron Beam Accelerator Facility (CEBAF) Large Acceptance Spectrometer (CLAS) at Jefferson Lab [12]. CLAS is a large-acceptance spectrometer used to detect multiparticle final states. Six superconducting coils generate a toroidal magnetic field around the target with azimuthal symmetry about the beam axis. The coils divide CLAS into six sectors, each functioning as an independent magnetic spectrometer. Each sector is instrumented with three regions of drift chambers (DCs), R1-3, to determine charged-particle trajectories [13], and scintillator counters (SCs) for time-of-flight measurements [14]. In the forward region, gas-filled threshold Cherenkov counters (CCs) are used for electron and/or pion separation up to 2.5 GeV [15],

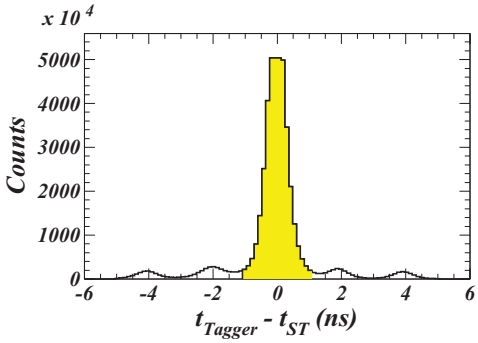

FIG. 3. (Color online) Difference between the Tagger time and the start-counter (ST) time (solid histogram). The tagger and ST coincidence time for selected events is required to be within 1 ns (shaded histogram). The secondary peaks, corresponding to the nearby beam buckets, are also visible.

and electromagnetic calorimeters (ECs) are used to identify and measure the energy of electrons and high-energy neutral particles, as well as to provide electron and/or pion separation [16]. The primary 1.645 GeV electron beam was incident on the thin radiator of the Hall-B photon tagger [17]. Tagged photons were produced with 20%–95% of the energy of the primary electron beam. In the g3a experiment, real photons tagged in the energy range from 0.35 to 1.55 GeV were incident on an 18-cm-thick liquid ^{3}He target. The field of the CLAS toroidal magnet was set to half of its maximum value to optimize the momentum resolution and the acceptance for positively charged particles. A trigger was used with a required coincidence between hits in the tagger, the start counter (ST), and the time-of-flight (TOF) paddles. About 10^9 triggers were collected at a production current of 10 nA.

B. Event selection

In order to associate the reaction of interest with the triggering tagged photon, the coincidence time between the tagger and CLAS was required to be within ± 1 ns. A cut was applied to the time difference Δt between the CLAS start time at the interaction point recorded by the start counter (ST) and the tagger. The central peak in Fig. 3 corresponds to the tagger hits that are in time coincidence with CLAS within the 2-ns-wide beam bucket. In the g3a run period, only about 2% of the events contained more than one tagged photon.

The final-state particles were identified by determining their charge, momentum, and velocity. Charge and momentum were obtained from the drift-chamber tracking information and the velocity from the time of flight and path length to the scintillation counters. Figure 4 shows the reconstructed mass distribution of positively charged particles. The events of interest were those with two and only two positively charged particles detected in coincidence. A triton candidate was required to have a positive charge and a reconstructed mass squared m^2 between 6.5 and 10.0 $(\mathrm{GeV}/c^2)^2$. A pion candidate was required to have a positive charge and a reconstructed mass squared between 0.05 and 0.3 $(\mathrm{GeV}/c^2)^2$. In order to assure that the events of interest were produced within the ^{3}He target

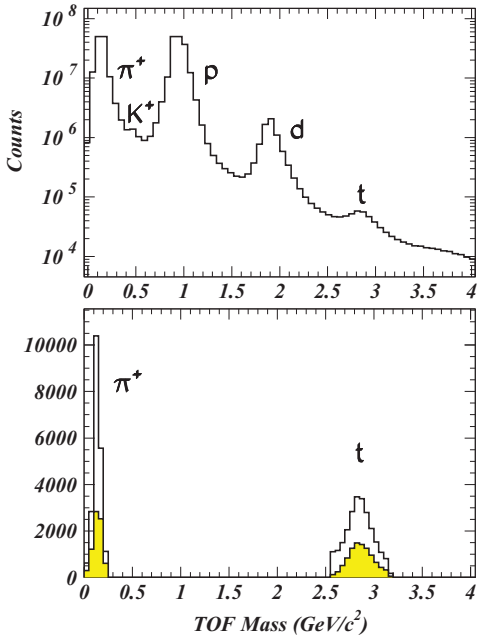

FIG. 4. (Color online) Hadron mass calculated from the time-of-flight information. The histogram in the top panel shows the mass distribution for all positively charged hadrons. The solid histogram in the lower panel is the selected sample of pions and tritons that are detected in coincidence. The shaded histogram shows the same distribution after applying all the kinematical cuts to remove the background (see Sec. III C for details).

volume, a cut was applied to the z component of the interaction vertex along the beam line.

Energy-loss corrections were applied to the selected particles because they lose a non-negligible part of their energy

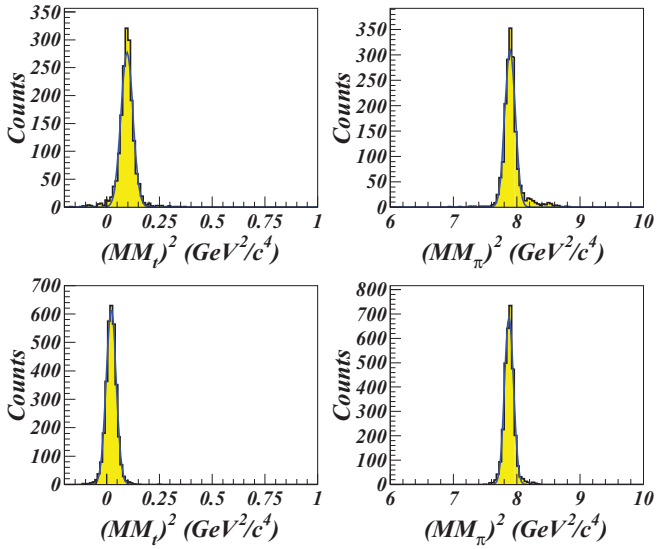

FIG. 5. (Color online) Distributions of the missing mass squared of the detected triton (left) and pion (right) before (top) and after (bottom) the energy-loss corrections. Gaussian fits shown in solid blue are performed to determine the mean value and the width of each distribution. The accepted values for the pion and triton mass squared are 0.0195 and 7.890 $(\mathrm{GeV}/c^2)^2$, respectively.

TABLE I. Summary of the mean values and widths of the pion and triton missing-mass-squared distributions before and after the energy-loss corrections. The accepted values for the pion and triton mass squared are 0.0195 and 7.890 $(\mathrm{GeV}/c^2)^2$, respectively.

	Without corrections	With corrections
$(MM_{\pi^+})^2$ $(\mathrm{GeV}/c^2)^2$	7.894	7.878
Width $(\mathrm{GeV}/c^2)^2$	0.08197	0.06974
$(MM_t)^2$ $(\mathrm{GeV}/c^2)^2$	0.09613	0.02137
Width $(\mathrm{GeV}/c^2)^2$	0.02846	0.02376

in the target material and start counter before they reach the drift chambers. The effect of the energy-loss corrections after applying all of the kinematic cuts on the final sample of $t\pi^+$ data is shown in Fig. 5. The importance of these corrections can be demonstrated by comparing the missing-mass squared of either the detected pion or the detected triton before and after applying these corrections. Table I summarizes the result of fitting Gaussians to the pion and triton missing-mass-squared distributions before and after the energy-loss corrections.

Also, fiducial-volume cuts were applied to ensure that the particles are detected within those parts of the volume of CLAS where the detection efficiency is high and uniform. These cuts select regions of CLAS where simulations reproduce the detector response reasonably well.

C. Background corrections

In order to cleanly select the $\gamma\,^3\mathrm{He} \rightarrow t\pi^+$ channel, two-body kinematics were used. The two-body final-state kinematics for real events require that the missing energy, missing momentum, and missing-mass squared for $t\pi^+$ events be zero. Also, the opening angle between the three vectors of the detected pion and triton $\theta_{t\pi^+}$ should be close to 180° in the center-of-mass frame. Our initial sample of events contains two and only two charged particles. Four-vector conservation for the reaction $\gamma\,^3\mathrm{He} \rightarrow t\pi^+$ leads to the determination of three kinematic variables — the missing energy E_X, the missing momentum P_X, and the missing-mass squared $M_X^2 = E_X^2 - P_X^2$. These kinematic variables are plotted in Fig. 6. For the real coherent $t\pi^+$ events, we then have $E_X = 0$ GeV, $P_X = 0\,\mathrm{GeV}/c$, $M_X^2 = 0\,(\mathrm{GeV}/c^2)^2$, and $\theta_{t\pi^+} = 180°$. Indeed, in Fig. 6 one can see clear peaks showing the real coherent $t\pi^+$ events. However, some background can be seen in the selected events. These events (mostly due to the $t\pi^+\pi^0$ channel) can be removed by applying additional kinematic cuts as follows:

(i) The first cut is applied to the difference between the measured scattering angle of the pion in the center-of-mass frame (from the measured three-momentum vector of the pion) and the calculated one from the conservation of the four momenta in the $\gamma\,^3\mathrm{He} \rightarrow t\pi^+$ reaction (by measuring only the triton momentum). This difference is plotted in the upper-left side of Fig. 7. The clear peak around zero corresponds to the real events from the coherent production of a pion and a triton. The events for which this angular difference is outside of the range [-0.1,0.1] were removed from the data.

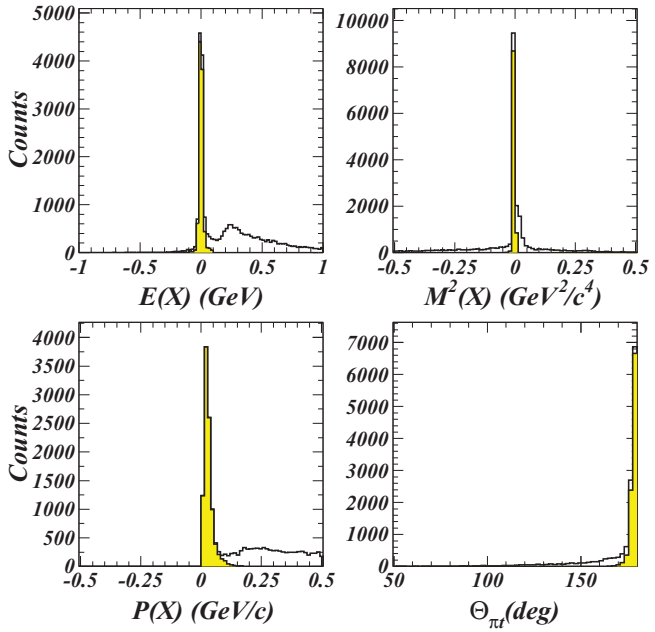

FIG. 6. (Color online) The π^+t two-body final-state kinematics require the missing energy (upper left), missing mass squared (upper right), and missing momentum (lower left) to be zero, and the π^+t opening angle (lower right) to be 180°. The peaks correspond to the real coherent π^+t events from the ^{3}He target. The shaded areas correspond to the nearly background-free sample of π^+t events after the five kinematical cuts described in the text were applied.

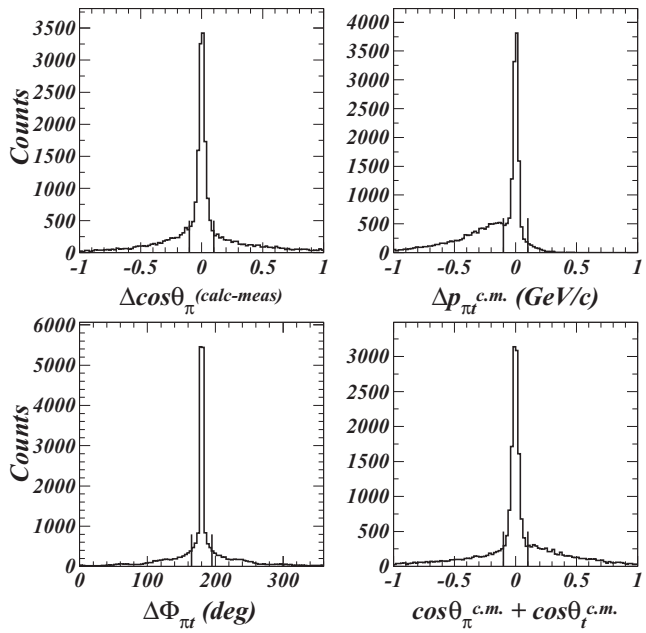

FIG. 7. Cuts were applied on various kinematical variables to remove the background. Upper left: The difference between the measured and calculated pion-scattering angles. Upper right: The difference between the magnitude of pion and triton momenta. Lower left: The difference between the pion and triton azimuthal angles. Lower right: The sum of the cosines of the pion and triton scattering angles. All quantities are shown in the center-of-mass frame.

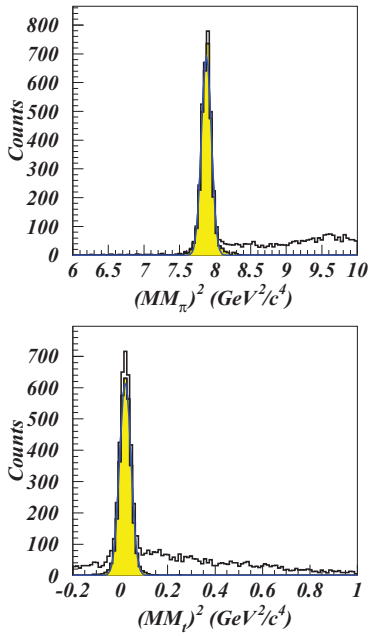

FIG. 8. (Color online) The calculated values for the missing mass squared for the detected pion (top) and the detected triton (bottom), before (solid histogram) and after (shaded histogram) applying the kinematic cuts. The background is removed by the kinematic cuts.

(ii) The second cut is applied to the difference between the momenta of the pion and the triton in the center-of-mass frame. For the real $t\pi^+$ events, this difference shows a peak at around zero with a tail that could be due to the $t\pi^+\pi^0$ events, as shown in the upper-right panel of Fig. 7. The applied cut requires this difference to be between -0.1 and 0.1 GeV/c.

(iii) The third cut requires the pion and triton three-momenta to be in the same plane as the initial photon, i.e., the difference between the azimuthal angles for the pion and the triton in the center-of-mass frame is selected to be $165^\circ < \phi^{\text{c.m.}}_{t\pi^+} < 195^\circ$. This distribution is shown in the lower-left panel of Fig. 7. A prominent peak at around 180° is clearly seen.

(iv) The fourth cut is applied to the sum of the cosines of the pion- and triton-scattering angles in the center-of-mass frame, shown in the lower-right panel of Fig. 7. This cut retains only those events with $-0.1 < \cos\theta^{\text{c.m.}}_{\pi} + \cos\theta^{\text{c.m.}}_{t} < 0.1$.

(v) Finally, the fifth cut requires the $t\pi^+$ missing energy to be $-0.1 < E(X) < 0.1$ GeV, shown in the upper left panel of Fig. 6.

The value of each of these cuts is optimized such that the maximum number of "good" $t\pi^+$ events is retained. Using these cuts, the background in the spectra of the previously described kinematic variables is mostly removed, as can be seen for the shaded areas of Fig. 6. The sample of events used after these cuts is nearly background-free. This is further supported by calculating the missing-mass squared of either the detected pion or the detected triton. These distributions are shown before and after the above cuts in Fig. 8, and show that the background has been removed. The clean sample of pions and tritons that are detected in coincidence is also shown within the shaded areas of Fig. 4.

TABLE II. Summary of kinematic cuts for event selection.

Description	Cut
Coincidence time Δt	<1 nsec
Positively charged particles	2
Pion identification	$-0.06 < m^2_\pi < 0.05$ (GeV/c^2)^2
Triton identification	$6.5 < m^2_t < 10.0$ (GeV/c^2)^2
z vertex	[-8,7.5] (cm)
$\Delta\cos\theta^{\text{c.m.}}_{\pi}$	[-0.1,0.1]
$\Delta p^{\text{c.m.}}_{\pi,t}$	[-0.1,0.1] (GeV/c)
$\Delta\phi^{\text{c.m.}}_{\pi,t}$	[165,195] deg
$\cos\theta^{\text{c.m.}}_{\pi} + \cos\theta^{\text{c.m.}}_{t}$	[-0.1,0.1]

Table II summarizes the final cuts used to identify the $t\pi^+$ events as described in this section.

D. Detector efficiency and acceptance

The raw $t\pi^+$ yields are obtained as a function of the photon-beam energy E_γ and the pion polar angle in the center-of-mass frame $\theta^{\text{c.m.}}_{\pi}$. The yields are corrected for the detector acceptance using a Monte Carlo simulation of phase-space-distributed $t\pi^+$ events within the entire 4π solid angle. The photon energy was generated randomly with a uniform distribution from 0.35 to 1.55 GeV. The standard GEANT-based CLAS simulation package [18] was used to simulate the detector response. The simulated events were

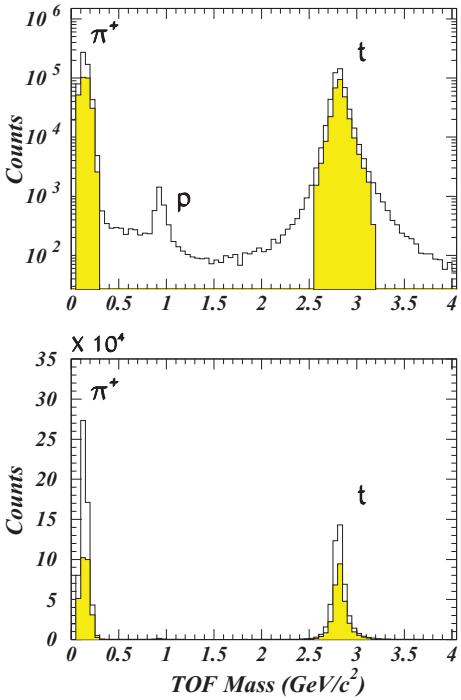

FIG. 9. (Color online) Simulated TOF masses for Monte Carlo generated events, plotted for both logarithmic (top) and linear (bottom) scales, before (solid histogram) and after (shaded areas) applying all of the cuts.

processed with the same event-reconstruction software that was used to reconstruct the real data. Figure 9 shows the reconstructed mass distributions for the simulated events with one pion and one triton after applying all of the cuts.

The acceptance is defined as the ratio of the number of reconstructed events to the number of generated events. Due to the geometry and the structure of CLAS, there are regions of solid angle that are not covered by the detector. Furthermore, the inefficiencies in the various components of the detector affect its acceptance and, consequently, the event reconstruction in CLAS. The acceptance correction factors are obtained as functions of pion angle $\theta_\pi^{\text{c.m.}}$ and photon energy E_γ for each kinematic bin and are used to convert the raw yields into un-normalized cross sections.

E. Cross sections

The differential cross section is obtained from the expression

$$\frac{d\sigma}{d\Omega} = \frac{N}{\eta_a N_\gamma N_T \Delta\Omega}, \tag{1}$$

where N is the number of measured events in a given energy and angular bin of solid angle $\Delta\Omega = 2\pi\,\Delta\cos\theta_{\text{c.m.}}$. The CLAS acceptance is given by η_a; N_γ is the number of photons within the given energy range incident on the target; and N_T is the number of target nuclei per unit area.

The number of target nuclei per unit area N_T is determined from

$$N_T = \frac{\rho l N_A}{A} \approx 2.089 \times 10^{-10}\ \text{nb}^{-1}, \tag{2}$$

where $l = 155.0$ mm is the target length, $\rho = 0.0675$ g/cm^3 is the density of liquid ^{3}He, $A = 3.016$ g/mol is its atomic weight, and $N_A = 6.022 \times 10^{23}$ atoms/mol is Avogadro's number.

The photon yield N_γ was obtained from the tagger hits using the GFLUX analysis package [19]. This number is corrected for the data-acquisition dead time.

F. Systematic uncertainties

Table III summarizes the systematic uncertainties. The uncertainty in the photon-flux determination, including the tagger-efficiency evaluation, is the same as in the g3a analysis of Niccolai *et al.* [11]. The value of the target density given in the literature was used; its uncertainty is no larger than 2%.

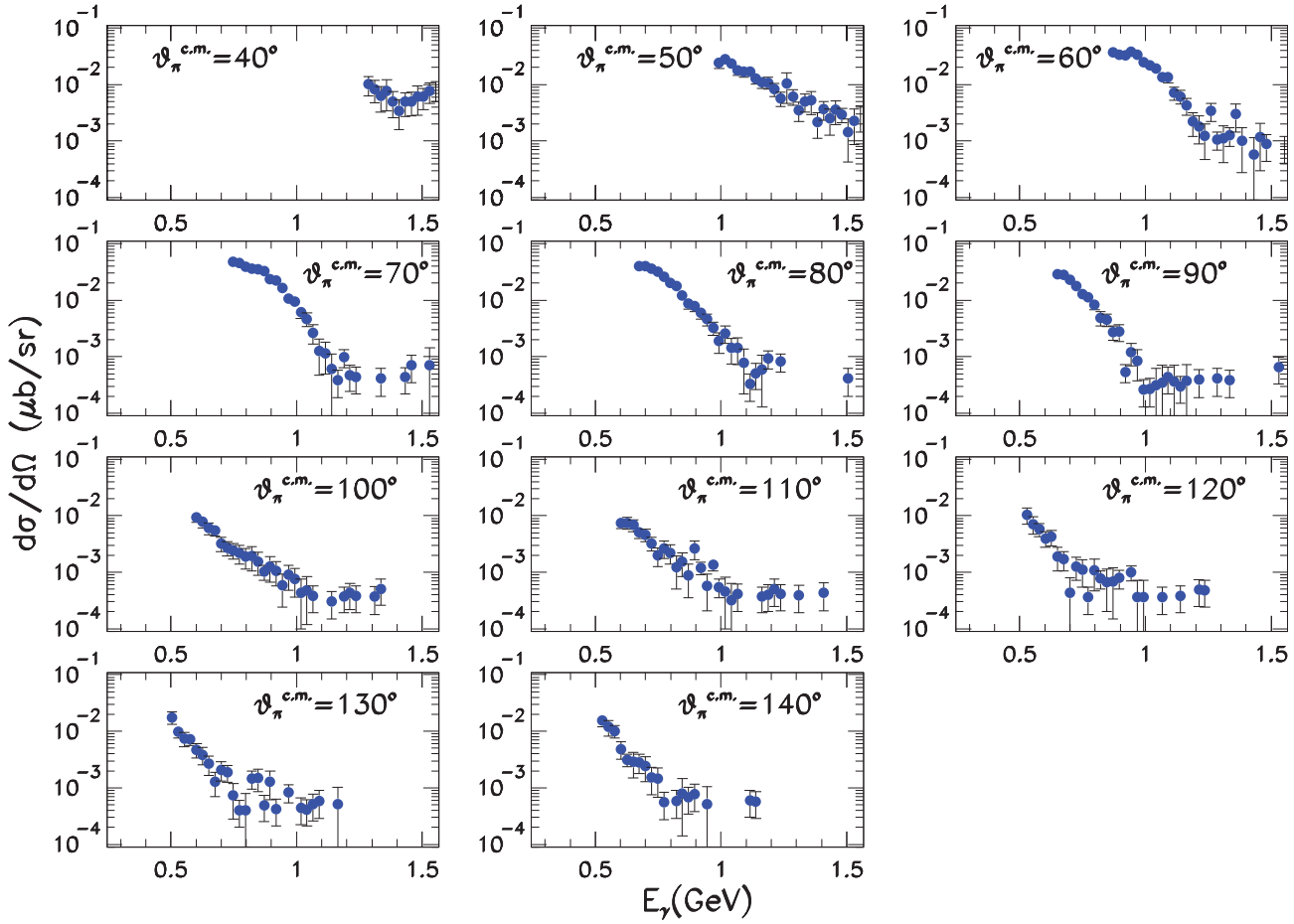

FIG. 10. (Color online) Measured differential cross sections as a function of E_γ for $\theta_\pi^{\text{c.m.}} = 40$, 50, 60, 70, 80, 90, 100, 110, 120, 130, and 140 deg. The error bars indicate statistical uncertainties only.

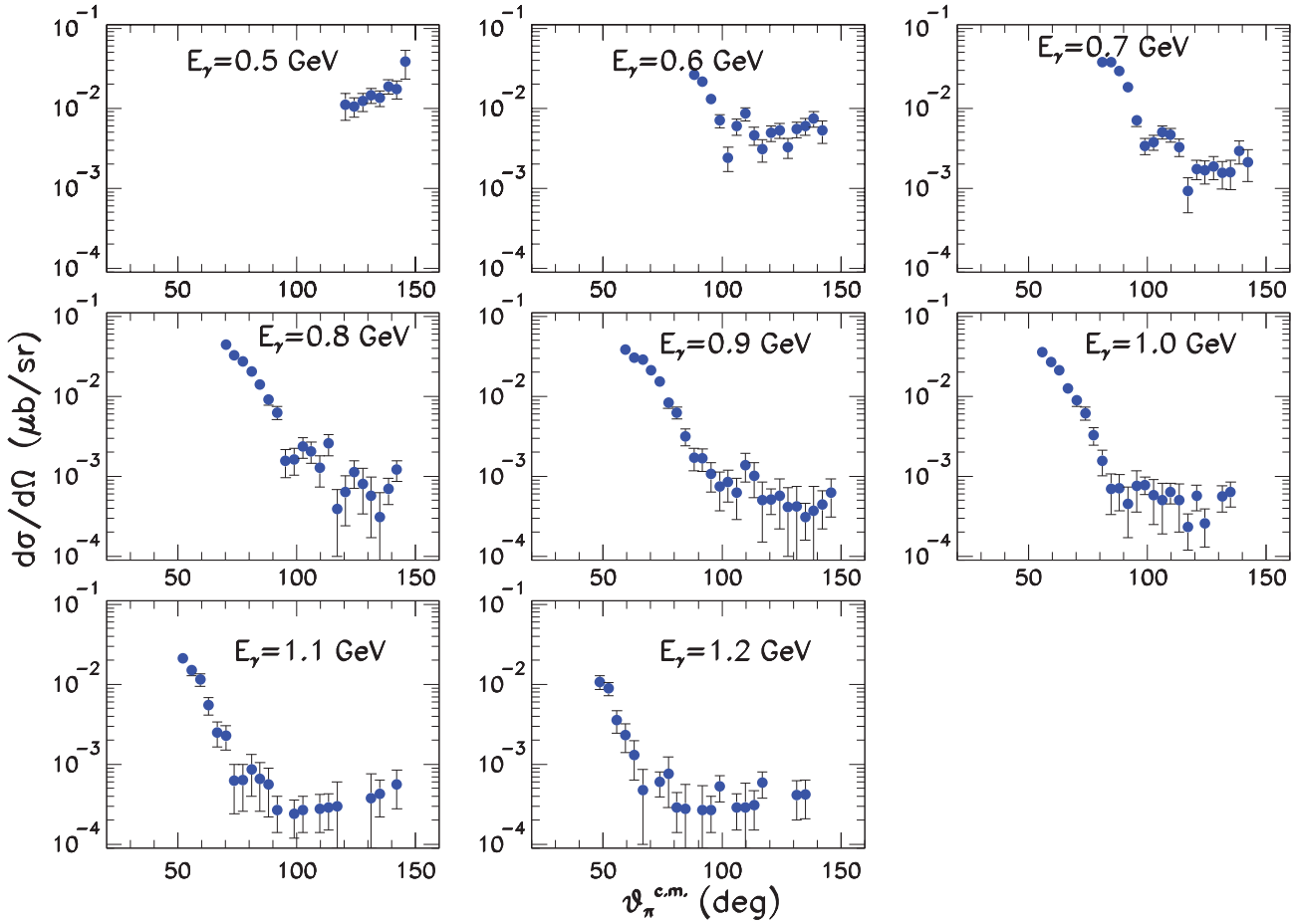

FIG. 11. (Color online) Measured differential cross sections as a function of $\theta_\pi^{\text{c.m.}}$ for $E_\gamma = 0.5$, 0.6, 0.7, 0.8, 0.9, 1.0, 1.1, and 1.2 GeV. CLAS acceptance limits the detection of the small angle pions. The error bars indicate statistical uncertainties only.

The uncertainties due to the fiducial cuts are estimated and have been found to be negligible.

The systematic uncertainty due to the CLAS acceptance was obtained by comparing the cross sections measured by each pair of the CLAS sectors independently (i.e., the data from sectors 1 and 4, 2 and 5, and 3 and 6 were combined). The mean deviation between the three sets of cross sections is given in Table III.

In order to estimate the systematic uncertainty due to applying the kinematic cuts, two sets of altered cuts, loose and tight, were used and compared with the nominal cuts. The root-mean-square of the distribution of the differences between the cross sections obtained with loose, tight, and the nominal cuts is considered to be a measure of the systematic uncertainty due to these cuts.

The CLAS acceptance and kinematic cuts constitute the largest part of the systematic uncertainty. The individual systematic uncertainties are summed in quadrature to less than 20%. The statistical uncertainties for the results of many kinematic bins are larger than the systematic uncertainties.

TABLE III. Summary of systematic uncertainties arising from various sources.

Source	Uncertainty (%)
Photon flux	6
Target density	<2
Fiducial cuts	Negligible
Solid angle	Negligible
CLAS acceptance	<15
Kinematic cuts	<10
Timing cut	Negligible
Total	<20

IV. RESULTS AND DISCUSSION

A. Cross sections

The measured differential cross sections are shown in Figs. 10 and 11 as functions of photon energy and pion angle, respectively. These plots show that the peak of the angular distributions shifts toward smaller angles with increasing photon energy. We have also studied the dependence of the cross sections on the momentum transferred to the triton, Q^2. This variable enters the nuclear wave functions and is mostly responsible for nuclear structure effects. Our measurements cover a range of $Q^2 = 10$–37 fm^{-2} [0.4–1.5 (GeV/c)^2] (see below).

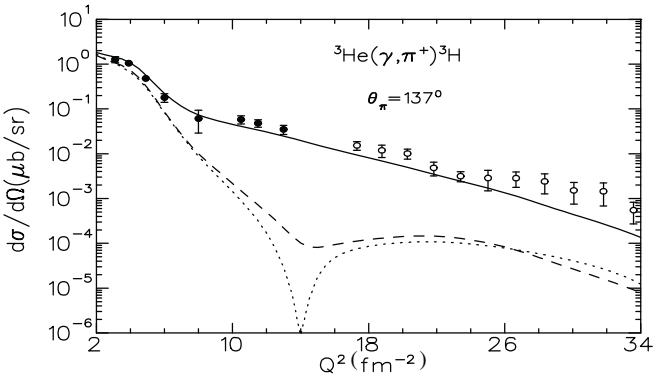

FIG. 12. Momentum-transfer dependence of the differential cross section for a fixed pion angle of 137 deg in the c.m. frame. The curves show the calculations by Tiator and Kamalov for three different assumptions: plane-wave impulse approximation PWIA (dotted lines); distorted-wave impulse approximation DWIA (dashed lines); and DWIA + two-body mechanism [10] (solid lines). Our data from CLAS are shown as open circles and from Ref. [3] as filled circles.

B. Comparison with model calculations and previous data

In this section our results are compared with the model calculations by Tiator and Kamalov and with previous measurements. The calculations were originally suited only for the energies from the threshold to the Δ resonance region. Recently this model has been extended (with MAID) to higher energies [20] (see Figs. 12–15). The curves show plane-wave impulse approximation PWIA (dotted line), distorted-wave impulse approximation DWIA (dashed line), and the DWIA + two-body mechanism [10](solid lines).

There is good agreement between the calculations and experimental data for small momentum transfers. For larger momentum transfers the calculations can describe the data only at backward angles. The old measurement at 137 deg can be nicely extended with our data up to $Q^2 = 34\ \mathrm{fm}^{-2}$ or $1.4\ \mathrm{GeV}^2$ (Fig. 12). For other angles a huge discrepancy is found, e.g., at 90 or 60 deg (Figs. 13 and 14). With the new elementary production operator from MAID, the agreement with data from

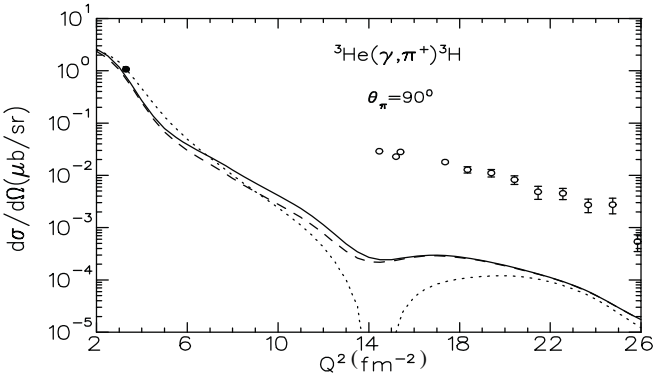

FIG. 13. Momentum-transfer dependence of the differential cross section for a fixed pion angle of 90 deg in the c.m. frame. The curves are described in Fig. 12. Our data from CLAS are shown as open circles and from Ref. [9] as a filled circle.

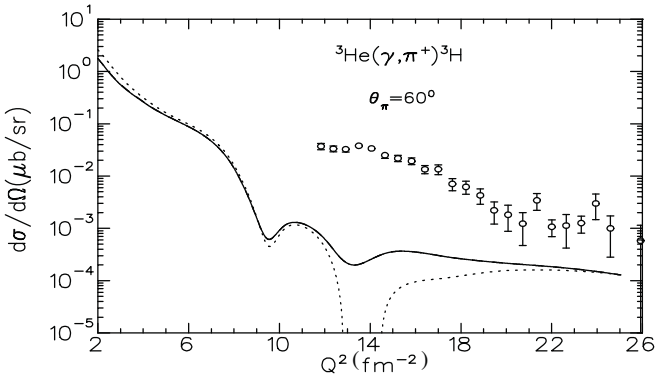

FIG. 14. Momentum-transfer dependence of the differential cross section for a fixed pion angle of 60 deg in the c.m. frame. The curves are described in Fig. 12. Our data from CLAS are shown as open circles. Note that in the forward direction, the DWIA and the DWI + two-body calculations coincide, as expected, so the two-body mechanism included in the model does not contribute.

Bachelier *et al.* [3] is much improved compared to the previous calculations in 1995 (see Fig. 2).

These are interesting results which were not observed before when only high-Q^2 data were available at one angle, namely, 137 deg. Our new data suggest that there are other mechanisms that produce much larger contributions than the one-body (impulse approximation) and the two-body mechanisms that were proposed in Ref. [10]. It is possible that two- or even three-body effects are driving the large cross sections, but it is not precisely known to what extent.

Figure 15 shows the comparison of the angular dependence of our cross sections with the full model calculations for four bins of photon energy from 0.5 to 0.8 GeV. In general, the calculations fail to describe our data at higher photon energies and forward angles. This suggests that the one- and two-body mechanisms alone cannot describe our data and that the discrepancy between the data and the calculation might be most likely due to the fact that the three-body mechanisms are not included in the model. In fact, strong evidence from analyzing CLAS data in other channels, for example, $\gamma\,^3\mathrm{He} \to ppn$ [11], $\gamma\,^3\mathrm{He} \to pd$ [21], and $\gamma\,^4\mathrm{He} \to pt$ [22], suggests that three-body contributions become more important, especially at $E_\gamma = 0.6{-}0.8$ GeV.

The models could be improved by including two-body and three-body MECs. These processes become more important, especially at high momentum transfers, because the momentum is shared between two or three nucleons.

Drechsel *et al.* [23] and Strueve *et al.* [24] also considered the two- and three-body MEC in their calculations for the ^{3}He and ^{3}H form factors. Both models described the experimental data with a good degree of success after including these processes.

Another possible process to include in the model would be the photoinduced reaction $\Delta(\gamma, \pi N)$ on a free Δ that is created from the $N + N \to \Delta + N$ reaction. The existence of these preformed Δ's was investigated by studying reactions such as $A(\gamma, \pi^+ p)B$. It was shown that the assumption of a small amount of preformed Δ can fit $^{12}C(\gamma, \pi^+ p)$ data from

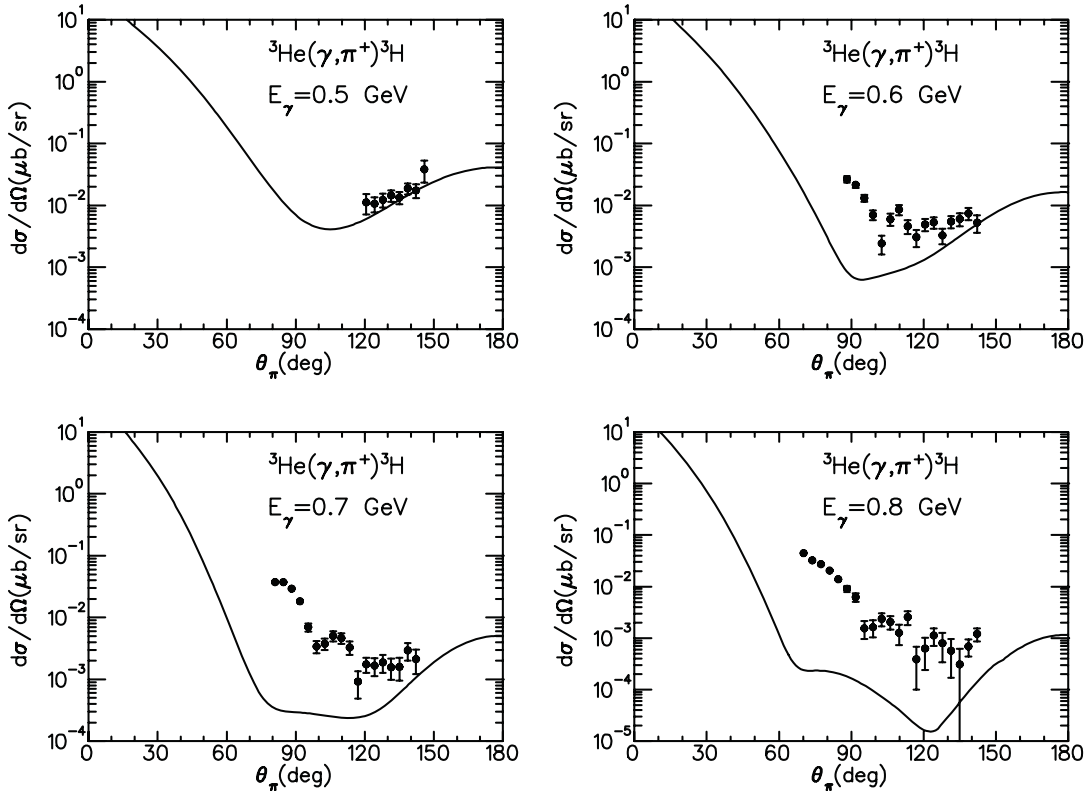

FIG. 15. Comparison of the model calculations from Tiator and Kamalov with the differential cross section as a function of pion scattering angle in the c.m. frame for various photon-energy bins. The model includes DWIA + two-body mechanism (see text).

MAMI if the Δ^{++} is in an $S_{\frac{3}{2}}$ orbital [25]. Preformed Δ's were also introduced in the calculations of the ^{3}He and ^{3}H form factors [24].

On the experimental side, it would be interesting to see whether there is a similar enhancement in the coherent π^0 photoproduction cross section at high momentum transfer from deuterium [26], ^{3}He, and ^{4}He targets. Perhaps data are available to be analyzed for this channel from various experimental groups, for example, Crystal Ball in Mainz, Crystal Barrel in Bonn, and CLAS at Jefferson Lab.

In summary, we have measured the differential cross section for the $\gamma^3\text{He} \to t\pi^+$ reaction in the energy range from 0.5 to 1.55 GeV for pion center-of-mass angles between 40 and 140 deg. We have compared our data with the results of the only available theoretical calculations for these energies [8,10,20]. The comparison shows that the calculations cannot describe our data at large momentum transfer and measured forward angles. This strongly suggests that there are additional production mechanisms that are not included in the current formulation of the model. It would certainly be interesting to see whether the coherent π^0 photoproduction shows similar effects.

ACKNOWLEDGMENTS

We would like to acknowledge the outstanding efforts of the staff of the Accelerator and the Physics Divisions at Jefferson Lab that made this experiment possible. This work was supported by the US Department of Energy under grant DE-FG02-95ER40901, the National Science Foundation, the Italian Istituto Nazionale di Fisica Nucleare, the French Centre National de la Recherche Scientifique, the French Commissariat à l'Energie Atomique, the National Reseach Foundation of Korea, the UK Science and Technology Facilities Council (STFC), and Scottish Universities Physics Alliance (SUPA). The Southeastern Universities Research Association (SURA) operated the Thomas Jefferson National Accelerator Facility for the United States Department of Energy under contract DE-AC05-84ER40150.

[1] J. R. O'Fallon *et al.*, Phys. Rev. **141**, 889 (1966).
[2] P. Argan *et al.*, Phys. Rev. C **20**, 242 (1979).
[3] D. Bachelier *et al.*, Phys. Lett. B **44**, 44 (1973); D. Bachelier *et al.*, Nucl. Phys. A **251**, 433 (1975).
[4] C. Lazard *et al.*, Nuovo Cimento A **16**, 605 (1973).
[5] B. Bellinghausen *et al.*, Nucl. Phys. A **470**, 429 (1987).
[6] J. L. Sanchez-Gomez and P. Pascual, Nucl. Phys. B **9**, 153 (1969).
[7] L. Tiator *et al.*, Nucl. Phys. A **333**, 343 (1980).
[8] S. S. Kamalov, L. Tiator, and C. Bennhold, Few-Body Syst. **10**, 143 (1991).
[9] N. d'Hose *et al.*, Nucl. Phys. A **554**, 679 (1993).

[10] S. Kamalov, L. Tiator, and C. Bennhold, Phys. Rev. Lett. **75**, 1288 (1995).
[11] S. Niccolai *et al.*, Phys. Rev. C **70**, 064003 (2004).
[12] B. A. Mecking *et al.*, Nucl. Instrum. Methods Phys. Res. A **503**, 513 (2003).
[13] M. D. Mestayer *et al.*, Nucl. Instrum. Methods Phys. Res. A **449**, 81 (2000).
[14] E. S. Smith *et al.*, Nucl. Instrum. Methods Phys. Res. A **432**, 265 (1999).
[15] G. Adams *et al.*, Nucl. Instrum. Methods Phys. Res. A **465**, 414 (2001).
[16] M. Amarian *et al.*, Nucl. Instrum. Methods Phys. Res. A **460**, 239 (2001).
[17] D. I. Sober *et al.*, Nucl. Instrum. Methods Phys. Res. A **440**, 263 (2000).
[18] CLAS GEANT Simulation [http://www.physics.unh.edu/maurik/Gsim/] (1997).
[19] J. Ball and E. Pasyuk, CLAS-NOTE 2005-002 (2005).
[20] L. Tiator and S. Kamalov (private communications, 2010).
[21] Y. Ilieva (private communications, 2010).
[22] R. Nasseripour *et al.*, Phys. Rev. C **80**, 044603 (2009).
[23] D. Drechsel *et al.*, Phys. Lett. B **108**, 159 (1982).
[24] W. Strueve *et al.*, Nucl. Phys. A **465**, 651 (1987).
[25] L. Wright and C. Chang, in Proceedings of the BLAST Workshop (2000) [http://citeseerx.ist.psu.edu/viewdoc/summary?doi=10.1.1.51.4522].
[26] Y. Ilieva *et al.*, Eur. Phys. J. A **43**, 261 (2010).